Joule

AI-assisted multi-objective hole-selective contact design for perovskite photovoltaics

Graphical abstract

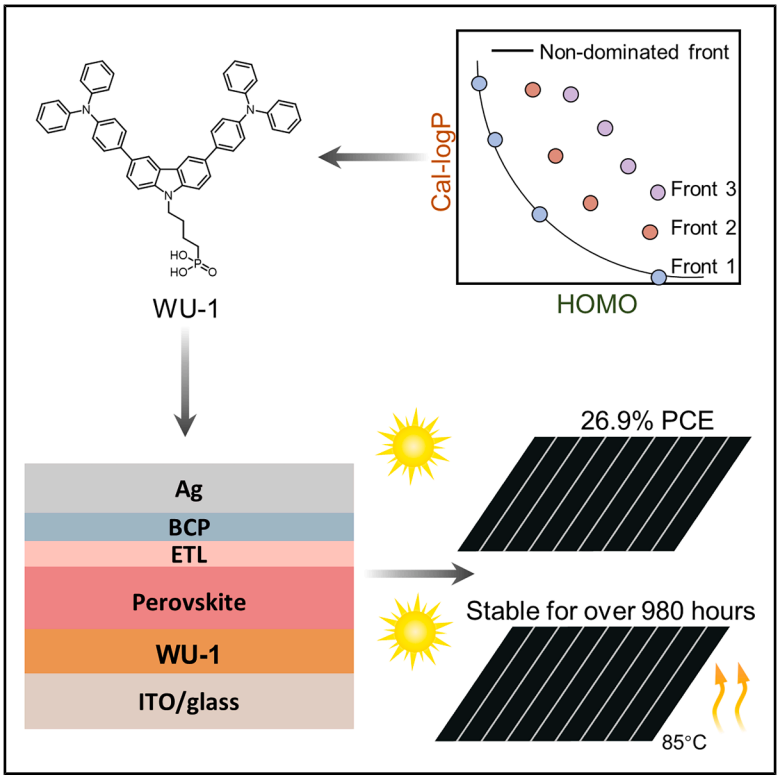

Highlights

- Developed AI-guided multi-objective design for high-performance HSCs
- Enabled efficient molecular space exploration through modular encoding
- Achieved 26.9% efficiency with thermal stability in WU-1-based devices

Authors

Yuejia Sun (孙悦嘉), Wei Fan (范唯), Qiqi Liu (刘奇奇), ..., Yaochu Jin (金耀初), Hanqing Jiang (姜汉卿), Rui Wang (王睿)

Correspondence

jinyaochu@westlake.edu.cn (Y.J.), hanqing.jiang@westlake.edu.cn (H.J.), wangrui@westlake.edu.cn (R.W.)

In brief

Designing functional materials for high-performance perovskite solar cells is often slow and a trial-and-error process. Here, we use surrogate-assisted multi-objective evolutionary algorithms to design molecules that improve both efficiency and stability at device interfaces. The approach identifies new molecules that enable perovskite solar cells to reach 26.9% efficiency with strong thermal stability. This work highlights how AI can accelerate the discovery of functional materials for next-generation energy technologies.

Sun et al., 2026, Joule *10*, 102497
October 21, 2026
https://doi.org/10.1016/j.joule.2026.102497

CellPress

Please cite this article in press as: Sun et al., AI-assisted multi-objective hole-selective contact design for perovskite photovoltaics, Joule (2026), https://doi.org/10.1016/j.joule.2026.102497

Joule

CellPress

Article

AI-assisted multi-objective hole-selective contact design for perovskite photovoltaics

Yuejia Sun (孙悦嘉),[1,2,6] Wei Fan (范唯),[1,2,6] Qiqi Liu (刘奇奇),[2,6] Jiahui Shen (沈嘉晖),[1,2,3,6] Pingdong Wei (卫平东),[2,6] Yuexin Liu (刘悦欣),[2,4] Qingqing Liu (刘情情),[2] Shaochen Zhang (张劭晨),[1,2] Jingjing Zhou (周晶晶),[2] Xiaonan Wang (王潇楠),[1,2] Xin Wu (武鑫),[5] Mengqi Han (韩梦琦),[5] Jingjing Xue (薛晶晶),[1] Bowen Zhu (朱博文),[2,5] Yaochu Jin (金耀初),[2,5,*] Hanqing Jiang (姜汉卿),[2,*] and Rui Wang (王睿)[2,5,7,*]

[1]School of Materials Science and Engineering, Zhejiang University, Hangzhou 310027, China

[2]School of Engineering, Westlake University, Institute of Advanced Technology, Westlake Institute for Advanced Study, Hangzhou 310024, China

[3]School of Chemistry and Chemical Engineering, Yangzhou University, Yangzhou 225002, China

[4]School of Physics, Dalian University of Technology, Dalian 116024, China

[5]Center for Interdisciplinary Research and Innovation, Muyuan Laboratory, 110 Shangding Road, Zhengzhou, Henan Province 450016, China

[6]These authors contributed equally

[7]Lead contact

*Correspondence: jinyaochu@westlake.edu.cn (Y.J.), hanqing.jiang@westlake.edu.cn (H.J.), wangrui@westlake.edu.cn (R.W.)

https://doi.org/10.1016/j.joule.2026.102497

CONTEXT & SCALE Inverted perovskite solar cells (PSCs) have achieved rapid efficiency improvements, but the design of molecule-based hole-selective contacts (HSCs) still relies heavily on experimental trial and error. Identifying molecules that simultaneously improve efficiency and operational stability remains challenging because device performance depends on multiple coupled interfacial properties. Here, we develop a data-efficient AI-guided strategy for HSC design. By combining modular molecular encoding with surrogate-assisted multi-objective evolutionary algorithms, we optimize the power conversion efficiency (PCE) and stability of the devices while minimizing the number of density functional theory calculations. The identified WU-series molecules deliver PCEs above 26%, with WU-1 reaching 26.9% and retaining 87% of its initial efficiency after 980 h of maximum power point tracking at 85°C under third-party tests. This work demonstrates that multi-objective AI optimization can accelerate interfacial molecule discovery and help connect molecular properties with device performance in perovskite photovoltaics.

SUMMARY

Inverted perovskite solar cells (PSCs) have advanced rapidly, with molecule-based hole-selective contacts (HSCs) emerging as key transport materials for forming relatively stable and uniform interfaces. However, summarizing the properties of well-performing molecules requires extensive experimental data. Here, we introduce an AI-guided strategy to identify promising molecules, minimizing the need for large-scale density functional theory calculations. We employ surrogate-assisted multi-objective evolutionary algorithms to simultaneously optimize the power conversion efficiency (PCE) and stability of the devices. The three molecules identified through this method demonstrate competitive PCEs exceeding 26% as hole-selective layers. Notably, the (4-(3,6-bis(4-(diphenylamino)phenyl)-9H-carbazol-9-yl)butyl)phosphonic acid (WU-1)-based solar cells achieved an impressive PCE of 26.9%. Under third-party tests, the WU-1-based device maintained 87% of its initial efficiency after 980 h of maximum power point tracking at 85°C. This multi-objective optimization framework provides a powerful tool for exploring the relationship between molecular properties and device performance, offering a new avenue for designing next-generation HSCs.

INTRODUCTION

Over the past decade, metal halide perovskite solar cells (PSCs) have achieved remarkable progress, with certified power conversion efficiencies (PCEs) reaching up to 27% in state-of-the-art inverted structures.[1–3] In these devices, transport layer materials are essential for modulating interfacial charge transport and enhancing both efficiency and long-term stability.[4,5] Among them, molecule-based hole-selective contacts (HSCs) have gained increasing attention because of their ability to form

Please cite this article in press as: Sun et al., AI-assisted multi-objective hole-selective contact design for perovskite photovoltaics, Joule (2026), https://doi.org/10.1016/j.joule.2026.102497

uniform and stable interfaces.[6–8] At present, the development of new HSCs largely relies on labor-intensive synthesis and characterization, guided by trends observed in high-performing molecular structures.[9–11] First-principles calculations are often employed to screen candidate materials, but these methods are computationally expensive, limiting the number of molecules that can be feasibly evaluated.[12,13] Alternatively, descriptor-based approaches, focusing on features such as dipole moments or energy levels, have shown potential for predicting device PCEs through structure-performance correlations.[14,15] However, these frameworks typically prioritize efficiency alone, require extensive experimental validation, and offer limited insight into long-term stability. While machine learning models are often used for prediction, they typically lack mechanisms for balancing multi-competing objectives during the design exploration and usually require large datasets[16] to achieve reliable performance.

To address these challenges, we present a data-efficient, AI-guided strategy that simultaneously optimizes multiple performance metrics, namely, PCE and operational stability of devices, based on the HSCs. We specifically investigate how the highest occupied molecular orbital (HOMO) level affects PCE and whether hydrophobicity correlates with improved operational stability, framing the problem as a multi-objective optimization (MOP).[17] To this end, we introduce surrogate-assisted multi-objective evolutionary algorithms (SA-MOEAs),[18–20] as a class of optimization techniques within AI tailored to settings with limited labeled data, which have recently emerged as powerful optimization frameworks for navigating large chemical spaces in functional materials discovery and inverse molecular design.[21–23] To further enhance synthetic accessibility, we develop a modular molecular encoding approach that decomposes HSCs into functionally meaningful fragments. Using two different SA-MOEA methods, we identified three promising HSC candidates, (4-(3,6-bis(4-(diphenylamino)phenyl)-9H-carbazol-9-yl)butyl)phosphonic acid (WU-1), (3-(3,6-bis(4-(diphenylamino)phenyl)-9H-carbazol-9-yl)propyl)-phosphonic acid (WU-2), and (8-(3,6-bis(4-(diphenylamino)-phenyl)-9H-carbazol-9-yl)octyl)phosphonic acid (WU-3), with fewer than 200 density functional theory (DFT) evaluations. All three candidates yielded PCEs above 26% in device integration, with WU-1 achieving a peak efficiency of 26.9%. Notably, WU-1-based PSCs maintained 93% of their initial efficiency after 2,000 h of maximum power point (MPP) tracking (MPPT) at 60°C. Under third-party testing at 85°C and 1-sun illumination, the same device retained 87% of its initial efficiency after 980 h. These results highlight a generalizable and data-efficient framework for molecular design in optoelectronic applications. While chemical intuition has played a central role in molecular design, it is also worth noting that our surrogate-based method alleviates the limitations of purely heuristic approaches by providing an optimization framework to assess which molecular properties contribute to PCE and operational stability. Our approach turns this into a well-defined optimization problem, allowing us to find experimentally validated candidates by using a limited number of DFT calculations. It offers a complementary and reproducible strategy that does not rely on subjective heuristics, and it not only accelerates the discovery of functional HSCs but also provides insight into key structure-performance relationships, offering a new path toward stable, high-efficiency PSCs.

RESULTS

Workflow of AI-guided multi-objective HSC design

We began by collecting 46 reported carbazole-based HSCs[24–26] rather than directly selecting molecules from large databases such as PubChem.[27] Each molecule is decomposed into four modular fragments in a puzzle-like scheme, with each fragment assigned a distinct identifier for unique encoding. Using this encoding system, we adopt Latin hypercube sampling (LHS) to generate 51 additional virtual HSCs, ensuring a more uniform exploration of the chemical space. The final dataset consists of 97 HSCs, including both the reported and newly generated structures (Figure 1A). Direct experimental evaluation of these targets for hundreds of candidates is time-consuming, requiring multi-step synthesis reactions, purification, and impractical device fabrication for each molecule. Therefore, we adopted the HOMO level and hydrophobicity, quantified by calculated logP (Cal-logp), as computationally accessible surrogate objectives that are expected to correlate with PCE and long-term stability, respectively. While these descriptors do not capture all aspects of device performance, they represent meaningful handles for molecular design. The difference in HOMO levels between HSCs and indium tin oxide (ITO)/perovskite interfaces is responsible for the hole injection efficiency of PSCs; HSCs with a suitable HOMO level that matches the perovskite valence band would significantly promote the charge extraction and reduce non-radiative recombination losses.[28] Meanwhile, recent studies have shown that interfacial modification can influence surface hydrophobicity in PSCs,[29,30] highlighting its role in tuning interfacial properties relevant to operational stability. These two keys, the HOMO level and Cal-logP values, are computed using DFT[31] and the Crippen surrogate model[32] in RDKit, respectively.

To investigate how the HOMO level influences PCE and whether hydrophobicity (as measured by Cal-logP) correlates with operational stability, we frame the molecular design as a bi-objective optimization problem. SA-MOEA is then applied to identify promising candidates. The process involves: (1) constructing surrogate models from the existing dataset, (2) performing a bi-objective evolutionary search based on model predictions, and (3) actively selecting new candidate molecules for DFT evaluation through a model management strategy. After the optimization, all evaluated molecules are ranked using non-dominated sorting, and top-ranking solutions are retained as potential molecules for synthesis (Figure 1B). Three candidate HSCs are selected from the archive of non-dominated solutions and synthesized. They are spin-coated onto ITO substrates and integrated into inverted PSCs with the structure ITO/HSC/perovskite/electron transport layer (ETL)/bathocuproine (BCP)/Ag. Among them, the best-performing device achieves a PCE of 26.9% and retains 87% of its initial efficiency after 980 h of MPPT at 85°C (Figure 1C). These experimental results validate the effectiveness of the entire AI-guided workflow and support our hypothesis regarding the relationships between the HOMO level and PCE and between hydrophobicity and operational stability.

Please cite this article in press as: Sun et al., AI-assisted multi-objective hole-selective contact design for perovskite photovoltaics, Joule (2026), https://doi.org/10.1016/j.joule.2026.102497

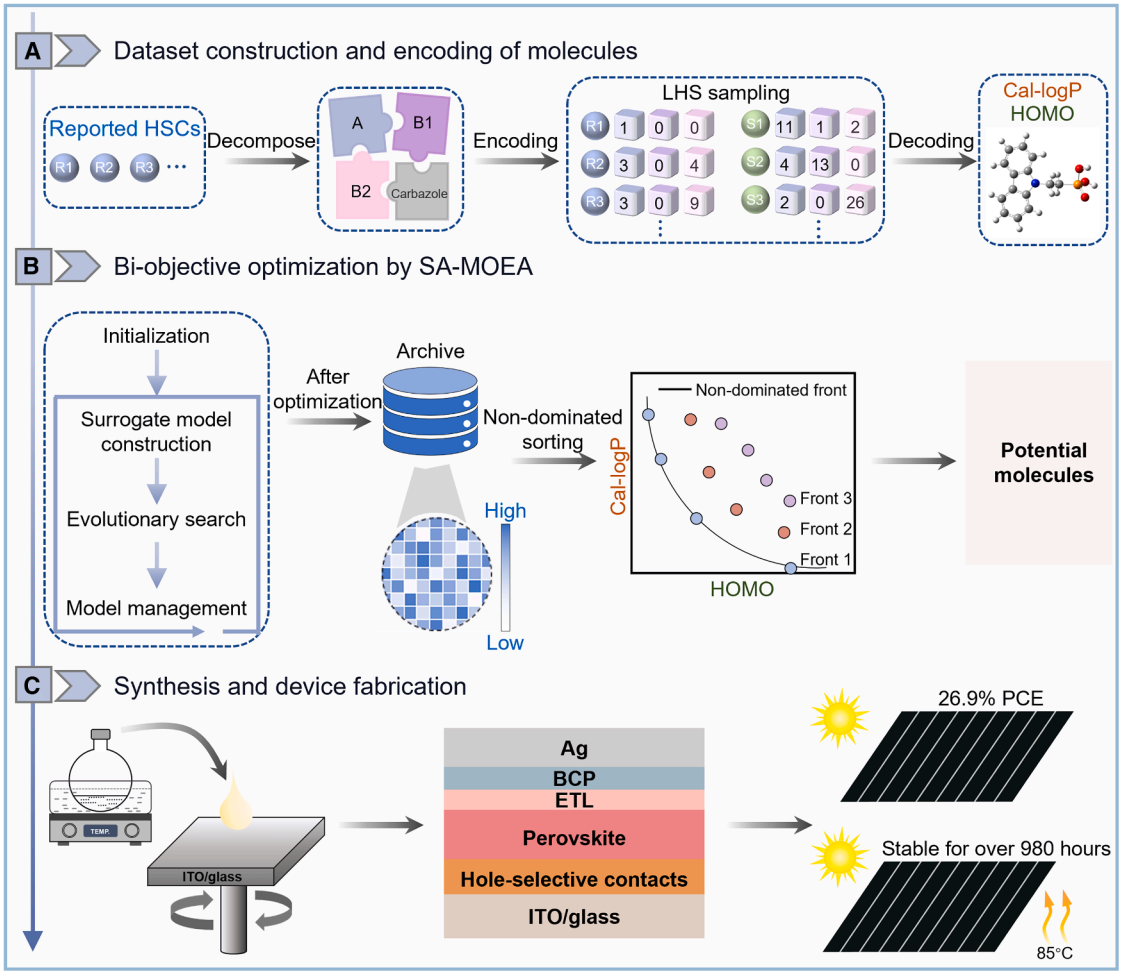

Figure 1. Overview of the AI-guided design approach for HSCs

(A) Reported carbazole-based HSCs are decomposed into structural fragments, enabling a modular digital encoding. LHS is used to generate additional HSCs to expand the dataset. The HOMO level values are computed via DFT, while Cal-logP values are estimated using the Crippen model, forming the basis for MOP.

(B) SA-MOEA is employed to optimize the HOMO level and Cal-logP values simultaneously. The process includes three iterative stages: surrogate model construction, evolutionary search, and model management. These steps are repeated to approach the true non-dominated front with minimal DFT evaluations. All evaluated molecules are stored and ranked via non-dominated sorting, and top-ranked candidates are selected for synthesis.

(C) Selected HSCs are synthesized and spin-coated onto ITO substrates to fabricate inverted PSCs, resulting in favorable device performance, including high efficiency and operational stability.

Step 1: Dataset construction and encoding of molecules

The first step in the AI-guided design of HSCs is the construction of an initial dataset based on modular encoding. Among known HSC candidates, carbazole-based molecules are the most widely reported[24] and have demonstrated superior performance in PSCs.[33–35] To enable effective data-driven molecular design, the carbazole-based phosphonic acid molecules remain the main family with a relatively extensive experimental dataset, while alternative anchoring groups such as boronic acids[36] and carboxylic acids[37] have limited device performance data and fewer validated molecular designs, making them unsuitable for data-driven exploration at this stage. We curated a set of high-performing carbazole-based HSCs from recent literature to serve as the seed for further exploration and optimization (Table S1).

In conventional molecular design of HSCs, molecules are commonly described using a three-part architecture consisting of anchoring, spacer, and terminal groups.[24,38,39] The anchoring group binds the molecule to the metal oxide substrate and determines interfacial stability and work function (WF). The spacer group connects the anchoring and terminal groups, influencing molecular packing and charge extraction characteristics. The terminal group directly interfaces with the perovskite layer, governing energy-level alignment for efficient hole extraction and defect passivation. While this structural description provides useful intuition for HSCs, it does not translate into a representation that can be directly used for data-driven exploration. To enable bi-objective optimization, we introduced a modular encoding strategy in which the carbazole unit serves as the core, with three fragments—fragment A, fragment B1, and fragment

Please cite this article in press as: Sun et al., AI-assisted multi-objective hole-selective contact design for perovskite photovoltaics, Joule (2026), https://doi.org/10.1016/j.joule.2026.102497

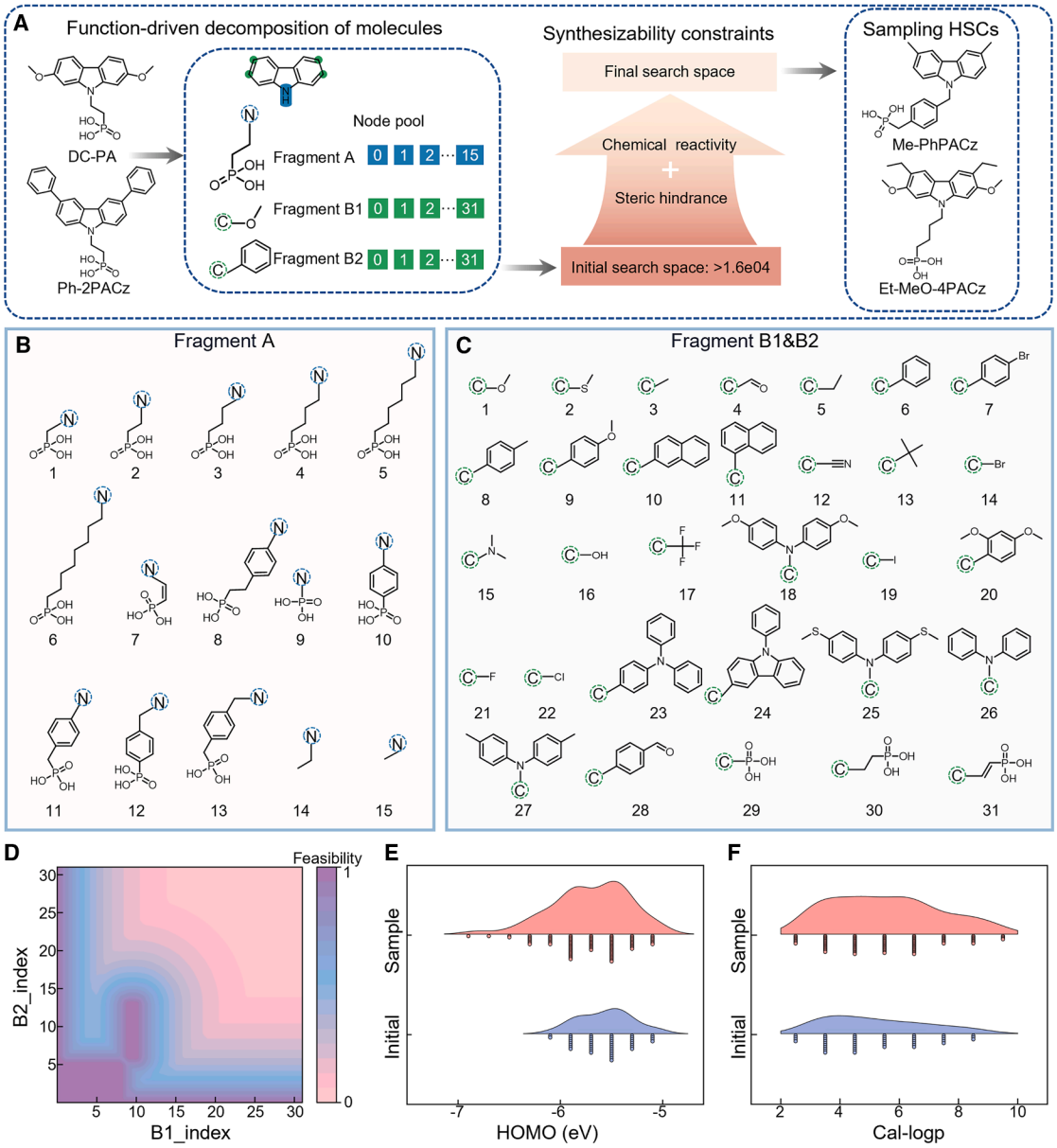

Figure 2. HSCs encoding and dataset construction

(A) HSCs are decomposed into three functional fragments—A, B1, and B2—and represented using a modular node-based encoding scheme. Each molecule is encoded as a three-digit numerical vector. To expand the dataset and improve chemical space coverage, new HSC candidates are generated via LHS, with synthetic feasibility constraints applied.

(B and C) Common fragments for A, B1, and B2 are summarized and assigned sequential indices to enable structured encoding.

(D) Feasibility map of fragment pairings (B1 and B2), illustrating regions that are chemically viable vs. synthetically challenging.

(E and F) Distribution of the HOMO level and Cal-logP values in the initial and LHS-augmented datasets, showing broader coverage after sampling.

B2—assembled around it (Figure 2A). Fragment A includes phosphonate groups with alkyl chains of varying lengths, typically providing anchoring functionality and connecting to the nitrogen atom of the carbazole ring. Fragments B1 and B2 correspond to substituents at the 2,7- and 3,6-positions of the carbazole, respectively,[40] both of which significantly influence the HOMO level and Cal-logP values. For example, in the (2-(2,7-dimethoxy-9H-carbazol-9-yl)ethyl)phosphonic acid) [DC-PA] molecule,[41] methoxy groups are present at the 2,7-positions, while in (2-(3,6-diphenyl-9H-carbazol-9-yl)ethyl)phosphonic acid (Ph2PACz),[42] phenyl groups are linked at the 3,6-positions. Substituents at other positions on the carbazole ring are ignored because of their lower reactivity. Only HSCs with a symmetric substituent at either the 2,7-position, 3,6-position, or both are considered. All known phosphonate-containing fragments and substituents are summarized and

Please cite this article in press as: Sun et al., AI-assisted multi-objective hole-selective contact design for perovskite photovoltaics, Joule (2026), https://doi.org/10.1016/j.joule.2026.102497

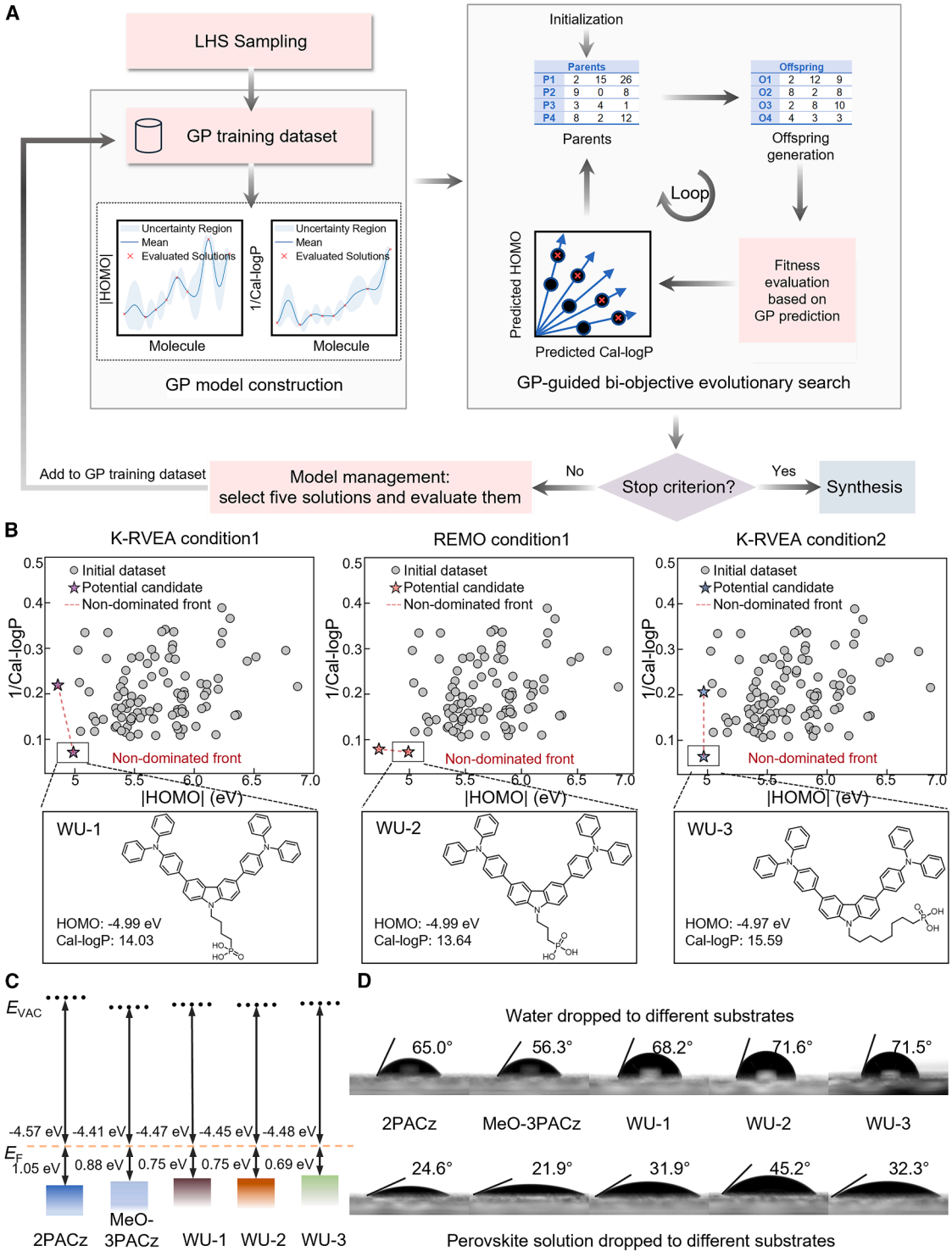

Figure 3. K-RVEA optimization workflow and experimental validation of HSC candidates

(A) Schematic of the K-RVEA-based surrogate-assisted MOP framework, consisting of GP model construction, GP-guided evolutionary search, and model management.

(legend continued on next page)

Please cite this article in press as: Sun et al., AI-assisted multi-objective hole-selective contact design for perovskite photovoltaics, Joule (2026), https://doi.org/10.1016/j.joule.2026.102497

extended into a standardized node pool (Figures 2B and 2C), providing a systematic framework for encoding and decoding.

In certain cases, the phosphonate groups with alkyl chains are attached directly to carbon (e.g., 2,7- or 3,6-) rather than nitrogen positions.[43] These fragments affect both anchoring and molecular properties and are treated as part of B1 or B2 accordingly. Based on this encoding scheme, we constructed a node pool with 15 options for fragment A and 31 options each for fragments B1 and B2. Each molecule is uniquely encoded as a three-digit code (A, B1, B2), where a zero denotes the absence of a given fragment. Conversely, any combination of these integers can be decoded into a valid molecule. This modular system creates a combinatorial space of over 16,000 possible HSC structures. However, many of these are synthetically infeasible due to steric hindrance or chemical incompatibility between B1 and B2 fragments. To address this, we define feasible and infeasible regions within the (B1, B2) substitution space, based on literature knowledge and expert judgment (Figure 2D).[7,44,45] The detailed feasibility criteria are summarized in Methods S1. Despite the curated fragment library, the number of reported HSCs is limited and insufficient to span the entire decision space. Therefore, we applied LHS across the encoded fragment space to generate 51 additional virtual HSCs (Table S2). The detailed dataset curation and filtering procedure is provided in Methods S1. This strategy ensures broad coverage of the chemical space, with high sampling efficiency. The HOMO level and Cal-logP values for these sampled molecules are computed using DFT and the Crippen model, respectively.

As shown in Figures 2E and 2F, the sampled HSCs broaden the distribution of both the HOMO level and Cal-logP values, compared with the initial set, indicating improved coverage of the search space. The resulting dataset, consisting of 97 HSCs (46 reported and 51 sampled), serves as the foundation for downstream optimization, using the SA-MOEA framework, specifically the Kriging-assisted reference vector-guided evolutionary algorithm (K-RVEA).

Step 2: Workflow of the K-RVEA algorithm

Based on the constructed dataset, we employed K-RVEA to identify molecules that exhibit favorable trade-offs between the HOMO level and Cal-logP values, while minimizing the number of costly DFT evaluations. The K-RVEA framework consists of three main phases: (1) building a Gaussian process (GP) surrogate model for each objective, (2) performing a bi-objective evolutionary search guided by the GP predictions, and (3) implementing a surrogate model management strategy to balance exploration and exploitation through active infill of new solutions, as illustrated in Figure 3A.

We began by training two independent GP models, using the encoded molecular representations as their inputs: one for predicting the HOMO level values and another for Cal-logP values. These surrogate models allow for fast estimation of molecular properties, significantly reducing the computational cost compared with direct DFT calculations. The predictions from these GPs are then fed into a RVEA to carry out the bi-objective search within the K-RVEA framework. After each search iteration, a model management strategy selects a small set of promising molecules for real evaluation, where the HOMO level and Cal-logP values are computed via DFT and the Crippen model in RDKit, respectively. These new data points are added to the training set, and the GP models are retrained to refine their accuracy. This process, i.e., GP training, evolutionary search, and model updating, is repeated over ten rounds.

A key component of the surrogate management strategy is the selection of solutions based on prediction uncertainty and angle-penalized distance values. Solutions with a high degree of uncertainty are prioritized to enhance exploration of under-sampled regions, while those with high-angle-penalized distance values typically indicate better trade-offs between the HOMO level and Cal-logP values. By considering both uncertainty and performance, this strategy ensures a balanced search across the vast molecule search space. A schematic illustration of the adaptive infill selection mechanism is provided in Methods S1 and Figures S3 and S4. In each round, five representative individuals are selected for real DFT calculation and incorporated into the GP training set. After ten rounds, all evaluated molecules are archived, and non-dominated sorting is applied to obtain the final candidate set. These candidates are then analyzed to explore correlations between the HOMO level and PCE and between Cal-logP and operational stability. Final HSC candidates are chosen based on their computed performance and synthetic feasibility and are subsequently synthesized and tested experimentally. This iterative, surrogate-assisted workflow greatly improves design efficiency and reduces resource waste due to unproductive synthesis.

To evaluate the robustness and versatility of the optimization strategy, we conducted three independent runs under different conditions, including modifications to the initial search space and replacement of K-RVEA with another SA-MOEA algorithm, the relation model-based multi-objective evolutionary algorithm (REMO). Details of both algorithms; their comparison; and the systematic validation of predictive accuracy, uncertainty quantification reliability, and structural preference learning are provided in the supplemental information (Methods S1; Figures S1–S9; Tables S3–S5). Across the three optimization runs, six non-dominated molecules populate the final non-dominated front. From these, three molecules differing only in alkyl chain length are selected for synthesis (Figure 3B). These three molecules, named WU-1, WU-2, and WU-3, exhibit very similar HOMO level and Cal-logP values, confirming the algorithm's ability to repeatedly identify high-quality candidates. All three were successfully synthesized (see Methods S2 and Figure S10) and subjected to characterization for validation (Figures S11–S19). For comparison, 2PACz, a widely used

(B) Results from three independent optimization runs (two using K-RVEA and one using REMO), all yielding structurally similar candidate molecules that differ only in alkyl chain length.

(C) Energy band diagrams of 2PACz, MeO-3PACz, WU-1, WU-2, and WU-3 thin films, derived from UPS measurements.

(D) Optical images and contact angle measurements of water and perovskite precursor solution droplets on the surfaces of the HSC films, showing enhanced hydrophobicity in the WU-series candidates.

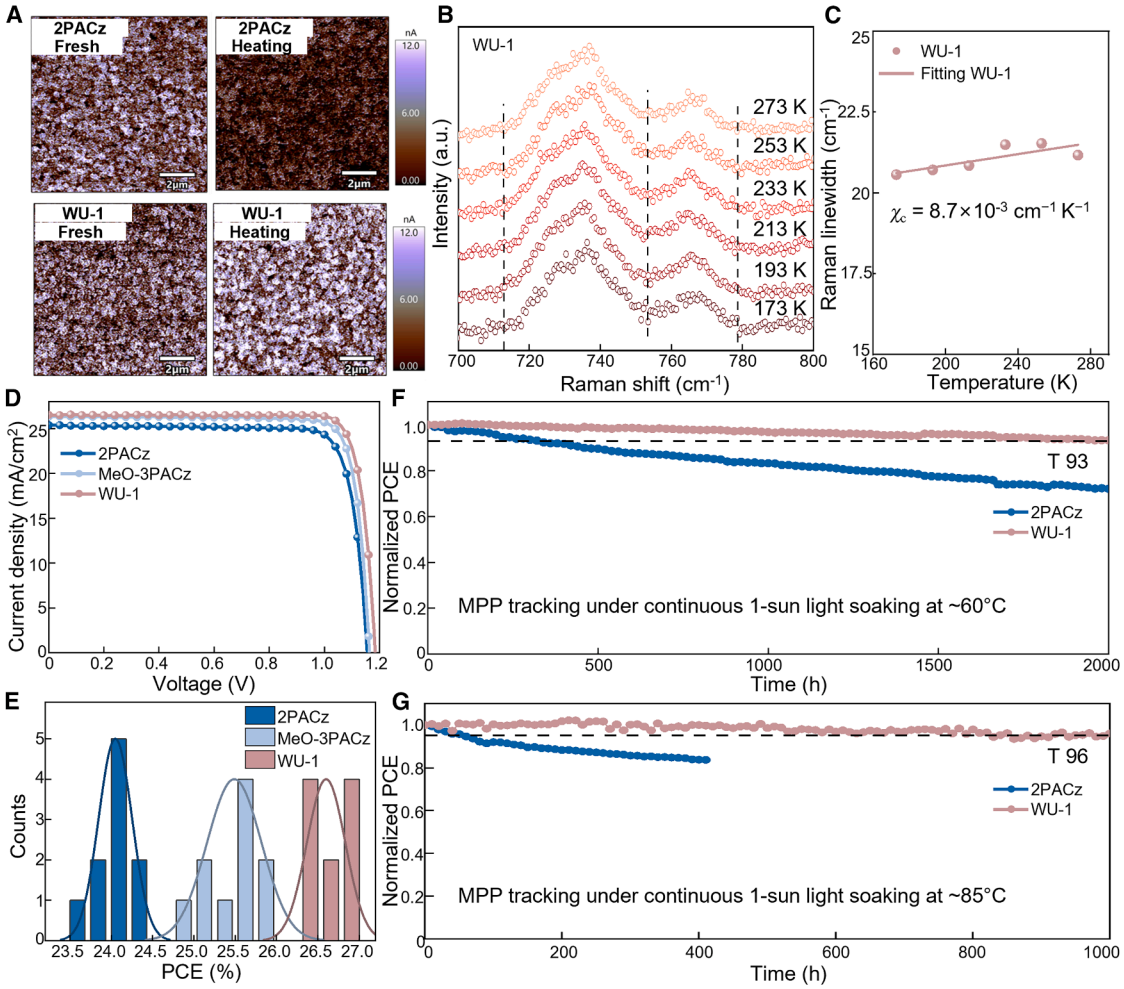

Figure 4. The enhanced efficiency and stability of the devices based on AI-assistedHSCs

(A) The c-AFM images of 2PACz films and WU-1 films before and after thermal aging in air at 120°C and 55% relative humidity (scale bars: 2 μm).

(B) Temperature-dependent Raman spectra of WU-1 recorded between 173 and 273 K.

(C) Temperature dependence of the Raman linewidth for the indicated vibrational modes of WU-1.

(D) The *J-V* curve of the best-performing cell fabricated by 2PACz, MeO-3PACz, and WU-1.

(E) The statistical distribution of the PCEs based on 2PACz, MeO-3PACz, and WU-1.

(F) The stability of the PCEs of WU-1- and 2PACz-based devices under MPPT at 60°C.

(G) The stability of the PCEs of the WU-1- and 2PACz-based devices under MPPT at 85°C.

benchmark HSC, and MeO-3PACz, a previously reported molecule located on the non-dominated front of the initially reported HSCs, were included as experimental references linking the predicted non-dominated front to experimentally validated HSC performance. To further demonstrate the generality of the framework, we also applied both K-RVEA and REMO to other objective sets under modified constraints. In all cases, final non-dominated fronts were obtained (Figure S20), indicating that the optimization workflow is adaptable to different but meaningful target definitions. As long as the objectives are formulated and computable, the SA-MOEA framework can effectively guide molecular design.

Ultraviolet photoelectron spectroscopy (UPS) was used to determine the surface energy levels of thin films deposited on ITO substrates (Figure S21). The WF values extracted from the UPS spectra are summarized in Figure S22, with values of 4.57 eV (2PACz), 4.41 eV (MeO-3PACz), 4.47 eV (WU-1), 4.45 eV (WU-2), and 4.48 eV (WU-3). The Fermi levels of 2PACz, MeO-3PACz, WU-1, WU-2, and WU-3 were −4.57, −4.41, −4.47, −4.45, and −4.48 eV, respectively; while the valence band maximum (VBM) values were −5.62, −5.29, −5.22, −5.20, and −5.17 eV (Figure 3C). Compared with 2PACz and MeO-3PACz, the WU-series molecules exhibit smaller gaps between the Fermi level and VBM, indicating enhanced p-type character. This observation aligns with the HOMO-shifting trend observed throughout the optimization and suggests improved hole extraction properties. The more favorable energy-level alignment between the WU-series and the perovskite valence band is expected to reduce the hole extraction barrier at the interface, thereby facilitating hole transport and suppressing interfacial

Please cite this article in press as: Sun et al., AI-assisted multi-objective hole-selective contact design for perovskite photovoltaics, Joule (2026), https://doi.org/10.1016/j.joule.2026.102497

non-radiative recombination.[46] Additionally, the increased CalogP values in WU-1, WU-2, and WU-3, achieved through SA-MOEA optimization, correlate with enhanced hydrophobicity. Contact angle measurements (Figure 3D) show reduced water and perovskite solution spreading on the WU-series films, compared with those formed by 2PACz and MeO-3PACz. Scanning electron microscopy (SEM) images and X-ray diffraction (XRD) patterns of perovskite films deposited on different HSCs (Figures S23 and S24) show comparable grain sizes and nearly identical diffraction features across all samples, indicating that the choice of HSC has a limited impact on perovskite crystallization under the current processing conditions. Therefore, the enhanced device performance is unlikely to originate from differences in film morphology or crystallinity but rather from improved interfacial properties, including optimized energy-level alignment and enhanced charge transport at the HSC/perovskite interface. To further elucidate the interfacial mechanisms, additional DFT calculations were performed, including both HSC/perovskite interface models and packed monolayer configurations. The results confirm stronger interfacial coupling and stable molecular packing for WU-1, supporting its favorable charge extraction properties and interfacial assembly (Figures S25 and S26; Methods S3). Together, these results confirm that the AI-guided optimization successfully identified HSCs that meet both electronic and interfacial performance targets and that the molecular structures discovered through K-RVEA and REMO translate reliably into experimentally observable improvements.

Photovoltaic performance

The conductive atomic force microscopy (c-AFM) monitoring of the current signals during the aging tests was conducted to examine the correlation between the AI-guided objectives and the stability of the perovskite devices. As shown in Figure 4A, thermal aging at 120°C in air (55% relative humidity) led to a notable drop in surface current for 2PACz films, while WU-1 films remained nearly unchanged, indicating enhanced stability. Improved stability was also observed for the WU-2 and WU-3 films (Figure S27). These results demonstrate that films formed using the AI-guided molecules possess significantly different stability characteristics, compared with those based on pre-optimization structures. This provides direct experimental evidence connecting molecular design strategies with device performance.

To investigate the vibrational dynamics of the assembled molecular structures, which are related to dynamical stability, temperature-dependent Raman spectroscopy was employed. As shown in Figure 4B, the ring folding-coupled modes of WU-1 near 734 and 766 cm^{-1} are highlighted. Very slight peak broadening was observed in WU-1 as the temperature increased from 173 to 273 K, a behavior attributed to anharmonic couplings between vibrons and phonons that became thermally populated upon heating.[47–49] The temperature-dependent linewidths of the scattering patterns are summarized in Figure 4C. All given linewidths represent the full width at half-maximum corresponding to Lorentzian line shapes. The temperature-dependent Raman linewidth behavior was simplified using a first-order linear approximation, where the slope reflects the coupling coefficient χc. In the case of the reference molecule 2PACz, the χc value was calculated as 3.1×10^{-2} cm^{-1} K^{-1}.[50] By comparison, the ring vibrational mode of WU-1 showed much weaker temperature-induced peak broadening ($\chi c = 8.7 \times 10^{-3}$ cm^{-1} K^{-1}), indicating suppressed anharmonic vibrational coupling and enhanced molecular rigidity under thermal perturbation.[50] The reduced thermal sensitivity of the Raman linewidth suggests that the vibrational structure of WU-1 remains comparatively stable upon heating, providing a plausible microscopic basis for the improved device stability observed at elevated temperatures. Given that interfacial instability and structural fluctuations can facilitate defect formation and promote ion migration pathways, the enhanced structural robustness of WU-1 is expected to suppress these degradation processes.

To evaluate the performance of WU-1, WU-2, and WU-3 employed as the HSCs in PSCs, we fabricated the devices based on the inverted structure ITO/HSC/$FA_{0.95}Cs_{0.05}PbI_3$/ETL/Ag, while the corresponding 2PACz- and MeO-3PACz-based devices were investigated in parallel for comparison. A champion PCE of 26.93% was achieved in the WU-1-based device (a stabilized PCE of 26.7%, Figure S17) for an aperture area of 0.075 cm^2 with an open-circuit voltage (V_{OC}) of 1.183 V, a short-circuit current density (J_{SC}) of 26.52 mA cm^{-2}, and a fill factor (FF) of 85.76% (Figure 4D). The external quantum efficiency (EQE) spectrum of the WU-1-based device is provided in Figure S28. The current density-voltage (*J-V*) curve shown in Figure 4D was obtained from the reverse scan; the corresponding forward scan *J-V* characteristics are provided in the supplemental information (Figure S29). The forward scan yields a PCE of 26.51%, with a V_{OC} of 1.184 V, J_{SC} of 26.56 mA cm^{-2}, and FF of 84.26%. The close agreement between the two scan directions indicates negligible hysteresis, suggesting low defect density and minimal interfacial ion accumulation. Dark *J-V* measurements (Figure S30) show a reduced reverse saturation current for WU-1, indicating suppressed interfacial recombination. Electrochemical impedance spectroscopy (EIS) measurements (Figure S31) reveal a smaller semicircle for WU-1-based devices, corresponding to reduced charge transfer resistance and improved interfacial charge transport. For the 2PACz- and MeO-3PACz-based devices in the same batch, we obtained, respectively, a PCE of 24.31% and 25.94% (stabilized 23.94% and 25.42%, Figure S32), V_{OC} of 1.155 and 1.163 V, J_{SC} of 25.39 and 26.32 mA cm^{-2}, and FF of 82.88% and 84.76%. Within the same batch, we fabricated the WU-2- and WU-3-based devices and achieved PCEs of 26.34% and 26.40% (Figure S33). These results highlight that the bi-objective (HOMO and Cal-logP) AI-guided design leads to HSC molecules with superior photovoltaic performance. Insights into the correlation between HSC molecules and photovoltaic performance can be developed through a systematic analysis of the selected design objectives. According to the statistical distribution of the PCEs (Figure 4E), the WU-1-based PSCs exhibited higher average values, verifying the superiority of WU-1 in achieving a high PCE (Figure S34 and Table S6 for detailed photovoltaic parameters).

To understand the improvement in the PCEs, we conducted the transient photocurrent (TPC) measurement under a short-circuit condition to delineate the carrier dynamics at the interface.

Please cite this article in press as: Sun et al., AI-assisted multi-objective hole-selective contact design for perovskite photovoltaics, Joule (2026), https://doi.org/10.1016/j.joule.2026.102497

The WU-1-based devices showed faster TPC decay, compared with the control devices, which suggests facilitated charge extraction at the interface (Figure S35). We measured the time-resolved photoluminescence (TRPL) of the perovskite film deposited on the molecular layers at a low laser fluence and derived the differential lifetime as shown in Figure S36. The first interval in the differential lifetime profile, which is dominated by the charge transfer, was shorter for WU-1, verifying its superior interfacial charge extraction, compared with 2PACz and MeO-3PACz.[51,52]

The stability of the perovskite devices was assessed under accelerated aging conditions according to the International Summit on Organic Photovoltaic Stability (ISOS) protocols.[53] We measured the devices in MPPT under simulated 1-sun illumination at ~60°C. The control device retained only ~70% of its initial PCE after 2,000 h of operation, whereas the WU-1-based device retained over 93% of its initial PCE (Figure 4F). Devices based on molecules pre- and post-machine learning optimization exhibited different stability performances, suggesting that the selected optimization objectives are in some way linked to enhanced device stability. We also performed the test at a higher temperature of 85°C; our target device retained over 93% of its initial PCE after 1,000 h of operation, and the 2PACz-based device retained about 84% after only 410 h (Figure 4G). We sent our device to a third-party organization for certification of the MPPT test at an elevated temperature of 85°C. As shown in Figure S37, the PCE of the device based on WU-1 remained over 87% after 980 h, justifying the potential of the long-term stability of the device. The devices based on pre- and post-optimization molecular structures showed remarkable differences in PSC performance. Such a clear contrast confirms the ability of our AI algorithm to relate the selected molecular design objective to device performance.

DISCUSSION

In this work, we developed an AI-guided, data-efficient multi-objective design framework for molecule-based HSCs in inverted PSCs by jointly optimizing the HOMO level and CaI-logP as computationally accessible surrogate objectives for efficiency and operational stability. A modular fragment-based encoding scheme, combined with LHS, enabled systematic expansion and exploration of the chemical space. Using SA-MOEA, we identified three candidates with fewer than 200 DFT evaluations. Experimentally, all three HSCs delivered PCEs above 26%, with WU-1 achieving a champion efficiency of 26.9% alongside improved interfacial charge extraction and film robustness. WU-1-based devices retained 93% of their initial efficiency after 2,000 h of MPPT at 60°C and 87% after 980 h of MPPT at 85°C in a third-party test. This MOP strategy links molecular properties to device performance in a practical and reproducible manner, providing a general workflow to discover stable, high-efficiency interfacial molecules for perovskite photovoltaics.

METHODS

Materials

All materials used in this work were obtained commercially and used without further purification, unless otherwise specified. The transparent ITO glass (10 Ω per square, transmittance 88%) was purchased from Shenzhen Huayu United Technology. The perovskite raw materials including lead iodide (PbI_2, purity 99.999%, perovskite grade), formamidinium iodide (FAI, purity 99.99%), methylammonium chloride (MACl, purity 99.9%), lithium fluoride (LiF, purity 99.99%), C_{60} (purity 99.9%), and Al_2O_3 dispersions (with a hydrated diameter of 30 nm, dispersed in ethanol) were all purchased from Advanced Election Technology. BCP (purity 99%), cesium iodide (CsI, purity 99.999%), MeO-3PACz (purity 99%), and oleylammonium iodide (OAmI, purity 99.5%) were purchased from Xi'an Yuri Solar. 2PACz (purity 98%) was obtained from Tokyo Chemical Industry. The required solvents including N,N-dimethylformamide (DMF, extra dry, purity 99.8%), dimethyl sulfoxide (DMSO, anhydrous, ≥99.9%), isopropanol (IPA, extra dry, purity 99.5%), methanol (extra dry, purity 99.8%), and chlorobenzene (CB, extra dry, purity 99.5%) were purchased from Sigma-Aldrich. Ag (purity 99.99%) was purchased from LiaoNing JiaYun High Technology.

Preparation of molecule solutions

For the preparation of molecule solutions, the molecule powders were fully dissolved in a mixed solvent of methanol and DMF at a volume ratio 3:1 at room temperature. The concentrations of 2PACz, MeO-3PACz, WU-1, WU-2, and WU-3 solutions are 2 mM.

Preparation of perovskite precursors and films

For the preparation of perovskite films with a composition $FA_{0.95}Cs_{0.05}PbI_3$, 1.65 M perovskite precursor solution was prepared by dissolving CsI, FAI, and PbI_2 in 1 mL mixed solvent of DMF and DMSO at a volume ratio 5:1. Additional 5 mol % PbI_2 and 10 mol % MACl were added to the precursor solution, and the solution was stirred overnight. The filtered perovskite precursor was then spin-coated on substrate at 1,000 rpm for 10 s and 5,000 rpm for 40 s in nitrogen glovebox. 200 μL of CB anti-solvent was dropped quickly at 25 s during the second spinning step. Afterward, the film was annealed at 125°C for 30 min.

Fabrication of inverted PSC devices

The pre-patterned ITO glasses (20 × 20 mm) were washed with detergent solution, deionized water, acetone, and IPA, each under 30 min of sonication, followed by drying with a pure nitrogen flow. The cleaned and dried ITO substrates were then treated with ultraviolet-ozone for 30 min before being transferred into glovebox filled with nitrogen. The molecule solution was spin-coated (Jiangsu Lebo Science Instrument) at 1,000 rpm for 10 s and 3,000 rpm for 40 s in the nitrogen glovebox. Afterward, the film was annealed at 115°C for 20 min. After cooling down to room temperature, 50 μL Al_2O_3 dispersion (diluted by 100 times) was spin-coated onto the molecular layers through the same recipe. Then perovskite films were coated on these layers following the abovementioned method. For the surface passivation layer, OAmI was dissolved in IPA with a concentration of 0.33 mg mL^{-1} and stirred at room temperature for 2 h. The OAmI solution was spin-coated on top of the as-prepared perovskite at 5,000 rpm for 30 s and then transferred to the hotplate and annealed at 100°C for 5 min.

After cooling down to room temperature, the whole device was transferred to a vacuum chamber under a base pressure of $<5.0 \times 10^{-6}$ Pa. 1.0 nm LiF at a rate of 0.1 Å s−1, 30 nm C_{60} at a rate of 0.3 Å s−1, and 6 nm BCP at a rate of 0.2 Å s−1 were thermally evaporated on the perovskite thin film sequentially (Angstrom Engineering, Beijing Technol Science), without breaking the vacuum. Finally, a 100-nm-thick Ag electrode at a rate of 1.5 Å s−1 was deposited to complete the devices for *J-V* measurements or stability tests.

RESOURCE AVAILABILITY

Lead contact

Requests for further information and resources should be directed to and will be fulfilled by the lead contact, Rui Wang (wangrui@westlake.edu.cn).

Materials availability

All unique/stable reagents generated in this study are available from the lead contact with a completed materials transfer agreement.

Data and code availability

- Data reported in this paper will be shared by the lead contact upon request.
- The source code for K-RVEA and REMO is publicly available in Zenodo at https://doi.org/10.5281/zenodo.19762839.
- Any additional information required to reanalyze the data reported in this paper is available from the lead contact upon request.

ACKNOWLEDGMENTS

The authors thank the High-Performance Computing Center for assistance with theoretical calculations and characterization support, and Z. Chen from the Instrumentation and Service Center for Molecular Sciences at Westlake University for assistance with characterizations. Funding: R.W. and J.X. acknowledge the grant LD24E020001 awarded by the Natural Science Foundation of Zhejiang Province of China. H.J. acknowledges support from the National Natural Science Foundation of China (grant 12350003). R.W. acknowledges a grant from the National Natural Science Foundation of China (grant number 62474143). R.W. acknowledges support from the Key R&D Program of Zhejiang (2024SSYS0061), the Zhejiang Key Laboratory of Low-Carbon Intelligent Synthetic Biology (2024ZY01025), and Muyuan Laboratory (program ID 14136022401). J.X. acknowledges the grant by the Natural Science Foundation of Zhejiang Province of China (LR24F040001), National Natural Science Foundation of China (grant no. 62274146). Y.J. acknowledges support from the International Collaboration Fund for Creative Research of the National Science Foundation of China (NSFC ICFCRT) under the grant no. W2441019. Qiqi Liu acknowledges support from the National Natural Science Foundation of China (grant 62302147).

AUTHOR CONTRIBUTIONS

R.W., H.J., Y.J., and J.X. conceived the idea. Y.S. and Qiqi Liu did the encoding strategy and evaluation algorithms for MOP; W.F. and Y.L. conducted the theoretical calculations; and W.F. and J.S. did the fabrication of perovskite films and devices. Qingqing Liu, X. Wu, and M.H. synthesized the WU-1, WU-2, and WU-3. Y.S., Qiqi Liu, W.F., J.S., P.W., Qingqing Liu, S.Z., J.Z., and X. Wang performed the data analysis under the supervision of R.W., H.J., and Y.J.. S.Z. and X. Wang assisted with the characterizations and device fabrication. J.X. and B.Z. provided helpful discussions. Y.S., W.F., Qiqi Liu, J.S., P.W., Y.J., H.J., and R.W. contributed to the interpretation of the results and wrote the manuscript. All the authors discussed the results and commented on the manuscript.

DECLARATION OF INTERESTS

The authors declare no competing interests.

SUPPLEMENTAL INFORMATION

Supplemental information can be found online at https://doi.org/10.1016/j.joule.2026.102497.

Received: December 18, 2025
Revised: March 27, 2026
Accepted: May 6, 2026

REFERENCES

1. Zheng, X., Hou, Y., Bao, C., Yin, J., Yuan, F., Huang, Z., Song, K., Liu, J., Troughton, J., Gasparini, N., et al. (2020). Managing grains and interfaces via ligand anchoring enables 22.3%-efficiency inverted perovskite solar cells. Nat. Energy *5*, 131–140. https://doi.org/10.1038/s41560-019-0538-4.
2. Chen, H., Liu, C., Xu, J., Maxwell, A., Zhou, W., Yang, Y., Zhou, Q., Bati, A.S.R., Wan, H., Wang, Z., et al. (2024). Improved charge extraction in inverted perovskite solar cells with dual-site-binding ligands. Science *384*, 189–193. https://doi.org/10.1126/science.adm9474.
3. Tan, Q., Li, Z., Luo, G., Zhang, X., Che, B., Chen, G., Gao, H., He, D., Ma, G., Wang, J., et al. (2023). Inverted perovskite solar cells using dimethylacridine-based dopants. Nature *620*, 545–551. https://doi.org/10.1038/s41586-023-06207-0.
4. Park, S.M., Wei, M., Lempesis, N., Yu, W., Hossain, T., Agosta, L., Carnevali, V., Atapattu, H.R., Serles, P., Eickemeyer, F.T., et al. (2023). Low-loss contacts on textured substrates for inverted perovskite solar cells. Nature *624*, 289–294. https://doi.org/10.1038/s41586-023-06745-7.
5. Wu, J., Yan, P., Yang, D., Guan, H., Yang, S., Cao, X., Liao, X., Ding, P., Sun, H., and Ge, Z. (2024). Bisphosphonate-Anchored Self-Assembled Molecules with Larger Dipole Moments for Efficient Inverted Perovskite Solar Cells with Excellent Stability. Adv. Mater. *36*, 2401537. https://doi.org/10.1002/adma.202401537.
6. Liu, J., Aydin, E., Yin, J., De Bastiani, M., Isikgor, F.H., Rehman, A.U., Yengel, E., Ugur, E., Harrison, G.T., Wang, M., et al. (2021). 28.2%-efficient, outdoor-stable perovskite/silicon tandem solar cell. Joule *5*, 3169–3186. https://doi.org/10.1016/j.joule.2021.11.003.
7. Qu, G., Cai, S., Qiao, Y., Wang, D., Gong, S., Khan, D., Wang, Y., Jiang, K., Chen, Q., Zhang, L., et al. (2024). Conjugated linker-boosted self-assembled monolayer molecule for inverted perovskite solar cells. Joule *8*, 2123–2134. https://doi.org/10.1016/j.joule.2024.05.005.
8. Tang, H., Shen, Z., Shen, Y., Yan, G., Wang, Y., Han, Q., and Han, L. (2024). Reinforcing self-assembly of hole transport molecules for stable inverted perovskite solar cells. Science *383*, 1236–1240. https://doi.org/10.1126/science.adj9602.
9. Zhu, J., Huang, X., Luo, Y., Jiao, W., Xu, Y., Wang, J., Gao, Z., Wei, K., Ma, T., You, J., et al. (2025). Self-assembled hole-selective contact for efficient Sn-Pb perovskite solar cells and all-perovskite tandems. Nat. Commun. *16*, 240. https://doi.org/10.1038/s41467-024-55492-4.
10. Wu, W., Gao, H., Jia, L., Li, Y., Zhang, D., Zhan, H., Xu, J., Li, B., Geng, Z., Cheng, Y., et al. (2025). Stable and uniform self-assembled organic diradical molecules for perovskite photovoltaics. Science *389*, 195–199. https://doi.org/10.1126/science.adv4551.
11. Zhang, Z., Duan, C., Wang, S., Xie, T., Zou, F., Luo, Y., Tang, R., Guo, K., Yuan, L., Zhang, K., et al. (2024). Molecular Design of Hole Transport Materials to Immobilize Ion Motion for Photostable Perovskite Solar Cells. Angew. Chem. Int. Ed. *63*, e202412042. https://doi.org/10.1002/anie.202412042.

12. Truong, M.A., Funasaki, T., Ueberricke, L., Nojo, W., Murdey, R., Yamada, T., Hu, S., Akatsuka, A., Sekiguchi, N., Hira, S., et al. (2023). Tripodal Triazatruxene Derivative as a Face-On Oriented Hole-Collecting Monolayer for Efficient and Stable Inverted Perovskite Solar Cells. J. Am. Chem. Soc. *145*, 7528–7539. https://doi.org/10.1021/jacs.3c00805.

13. Wu, T., Xu, X., Ono, L.K., Guo, T., Mariotti, S., Ding, C., Yuan, S., Zhang, C., Zhang, J., Mitrofanov, K., et al. (2023). Graphene-Like Conjugated Molecule as Hole-Selective Contact for Operationally Stable Inverted Perovskite Solar Cells and Modules. Adv. Mater. *35*, 2300169. https://doi.org/10.1002/adma.202300169.

14. Wu, J., Torresi, L., Hu, M., Reiser, P., Zhang, J., Rocha-Ortiz, J.S., Wang, L., Xie, Z., Zhang, K., Park, B.-W., et al. (2024). Inverse design workflow discovers hole-transport materials tailored for perovskite solar cells. Science *386*, 1256–1264. https://doi.org/10.1126/science.ads0901.

15. Wen, J., Yang, S., Jiang, L., Shi, Y., Huang, Z., Li, P., Xiong, H., Yu, Z., Zhao, X., Xu, B., et al. (2025). Accelerated discovery of high-performance small-molecule hole transport materials via molecular splicing, high-throughput screening, and machine learning. J. Mater. Inf. *5*, 30. https://doi.org/10.20517/jmi.2024.102.

16. Schneuing, A., Harris, C., Du, Y., Didi, K., Jamasb, A., Igashov, I., Du, W., Gomes, C., Blundell, T.L., Lio, P., et al. (2024). Structure-based drug design with equivariant diffusion models. Nat. Comput. Sci. *4*, 899–909. https://doi.org/10.1038/s43588-024-00737-x.

17. Hua, Y., Liu, Q., Hao, K., and Jin, Y. (2021). A survey of evolutionary algorithms for multi-objective optimization problems with irregular pareto fronts. IEEE/CAA J. Autom. Sin. *8*, 303. https://doi.org/10.1109/jas.2021.1003817.

18. Jin, Y., Wang, H., Chugh, T., Guo, D., and Miettinen, K. (2019). Data-Driven Evolutionary Optimization: An Overview and Case Studies. IEEE Trans. Evol. Comput. *23*, 442–458. https://doi.org/10.1109/TEVC.2018.2869001.

19. Chugh, T., Jin, Y., Miettinen, K., Hakanen, J., and Sindhya, K. (2018). A Surrogate-Assisted Reference Vector Guided Evolutionary Algorithm for Computationally Expensive Many-Objective Optimization. IEEE Trans. Evol. Comput. *22*, 129–142. https://doi.org/10.1109/TEVC.2016.2622301.

20. Hao, H., Zhou, A., Qian, H., and Zhang, H. (2022). Expensive Multiobjective Optimization by Relation Learning and Prediction. IEEE Trans. Evol. Comput. *26*, 1157–1170. https://doi.org/10.1109/TEVC.2022.3152582.

21. Liu, Y., Zhu, Y., Wang, J., Hu, R., Shen, C., Qu, W., Wang, G., Su, Q., Zhu, Y., Kang, Y., et al. (2025). A Multi-Objective Molecular Generation Method Based on Pareto Algorithm and Monte Carlo Tree Search. Adv. Sci. *12*, 2410640. https://doi.org/10.1002/advs.202410640.

22. Jablonka, K.M., Jothiappan, G.M., Wang, S., Smit, B., and Yoo, B. (2021). Bias free multiobjective active learning for materials design and discovery. Nat. Commun. *12*, 2312. https://doi.org/10.1038/s41467-021-22437-0.

23. Hoffman, S.C., Chenthamarakshan, V., Wadhawan, K., Chen, P.-Y., and Das, P. (2022). Optimizing molecules using efficient queries from property evaluations. Nat. Mach. Intell. *4*, 21–31. https://doi.org/10.1038/s42256-021-00422-y.

24. Han, P., and Zhang, Y. (2024). Recent Advances in Carbazole-Based Self-Assembled Monolayer for Solution-Processed Optoelectronic Devices. Adv. Mater. *36*, 2405630. https://doi.org/10.1002/adma.202405630.

25. Yao, Y., Cheng, C., Zhang, C., Hu, H., Wang, K., and De Wolf, S. (2022). Organic Hole-Transport Layers for Efficient, Stable, and Scalable Inverted Perovskite Solar Cells. Adv. Mater. *34*, 2203794. https://doi.org/10.1002/adma.202203794.

26. Wang, S., Guo, H., and Wu, Y. (2023). Advantages and challenges of self-assembled monolayer as a hole-selective contact for perovskite solar cells. Materials Futures *2*, 012105. https://doi.org/10.1088/2752-5724/acbb5a.

27. Xu, J., Chen, H., Grater, L., Liu, C., Yang, Y., Teale, S., Maxwell, A., Mahesh, S., Wan, H., Chang, Y., et al. (2023). Anion optimization for bifunctional surface passivation in perovskite solar cells. Nat. Mater. *22*, 1507–1514. https://doi.org/10.1038/s41563-023-01705-y.

28. Luo, D., Su, R., Zhang, W., Gong, Q., and Zhu, R. (2020). Minimizing non-radiative recombination losses in perovskite solar cells. Nat. Rev. Mater. *5*, 44–60. https://doi.org/10.1038/s41578-019-0151-y.

29. Cho, Y., Soufiani, A.M., Yun, J.S., Kim, J., Lee, D.S., Seidel, J., Deng, X., Green, M.A., Huang, S., and Ho-Baillie, A.W.Y. (2018). Mixed 3D–2D Passivation Treatment for Mixed-Cation Lead Mixed-Halide Perovskite Solar Cells for Higher Efficiency and Better Stability. Adv. Energy Mater. *8*, 1703392. https://doi.org/10.1002/aenm.201703392.

30. Shu, H., Xia, J., Yang, H., Luo, J., Wan, Z., Malik, H.A., Han, F., Yao, X., and Jia, C. (2020). Self-Assembled Hydrophobic Molecule-Based Surface Modification: A Strategy to Improve Efficiency and Stability of Perovskite Solar Cells. ACS Sustainable Chem. Eng. *8*, 10859–10869. https://doi.org/10.1021/acssuschemeng.0c02983.

31. Frisch, M.J., Trucks, G.W., Schlegel, H.B., Scuseria, G.E., Robb, M.A., Cheeseman, J.R., Scalmani, G., Barone, V., Petersson, G.A., Nakatsuji, H., et al. (2016). Gaussian 16 Rev, p. C.01.

32. Wildman, S.A., and Crippen, G.M. (1999). Prediction of Physicochemical Parameters by Atomic Contributions. J. Chem. Inf. Comput. Sci. *39*, 868–873. https://doi.org/10.1021/ci990307l.

33. Al-Ashouri, A., Magomedov, A., Roß, M., Jošt, M., Talaikis, M., Chistiakova, G., Bertram, T., Márquez, J.A., Köhnen, E., Kasparavičius, E., et al. (2019). Conformal monolayer contacts with lossless interfaces for perovskite single junction and monolithic tandem solar cells. Energy Environ. Sci. *12*, 3356–3369. https://doi.org/10.1039/C9EE02268F.

34. Liu, C., Yang, Y., Chen, H., Xu, J., Liu, A., Bati, A.S.R., Zhu, H., Grater, L., Hadke, S.S., Huang, C., et al. (2023). Bimolecularly passivated interface enables efficient and stable inverted perovskite solar cells. Science *382*, 810–815. https://doi.org/10.1126/science.adk1633.

35. Jiang, Q., Tirawat, R., Kerner, R.A., Gaulding, E.A., Xian, Y., Wang, X., Newkirk, J.M., Yan, Y., Berry, J.J., and Zhu, K. (2023). Towards linking lab and field lifetimes of perovskite solar cells. Nature *623*, 313–318. https://doi.org/10.1038/s41586-023-06610-7.

36. Guo, H., Liu, C., Hu, H., Zhang, S., Ji, X., Cao, X.-M., Ning, Z., Zhu, W.-H., Tian, H., and Wu, Y. (2023). Neglected acidity pitfall: boric acid-anchoring hole-selective contact for perovskite solar cells. Natl. Sci. Rev. *10*, nwad057. https://doi.org/10.1093/nsr/nwad057.

37. Ramasamy, A.K., Vasudevan, T., Rajamanickam, G., Chen, L.-C., and Chauhan, A.K. (2025). Synergistic Interface Engineering via Carboxylic-Acid-Functionalized Triphenylamine Derivative for High-Performance and Stable Perovskite Solar Cells. ACS Appl. Energy Mater. *8*, 7167–7181. https://doi.org/10.1021/acsaem.5c00532.

38. Zheng, Y., Niu, T., Chao, L., Xia, Y., and Chen, Y. (2025). Stability of hole-selective self-assembled monolayers in inverted perovskite solar cells. J. Energy Chem. *107*, 74–86. https://doi.org/10.1016/j.jechem.2025.03.032.

39. Ullah, A., Luo, Y., and De Wolf, S. (2026). Self-Assembled Monolayers in p–i–n Perovskite Solar Cells: Molecular Design, Interfacial Engineering, and Machine Learning–Accelerated Material Discovery. Adv. Mater. e20220. https://doi.org/10.1002/adma.202520220.

40. Degbia, M., Schmaltz, B., Van, F.T., Melhem, H., Bouclé, J., Tomkeviciene, A., and Grazulevicius, J.V. (2012). Comparative study of 2,7 versus 3,6 disubstituted carbazole as hole transporting materials in solid state DSSC. In 2012 International Semiconductor Conference Dresden-Grenoble (ISCDG), pp. 211–214. https://doi.org/10.1109/ISCDG.2012.6360014.

41. Deng, X., Qi, F., Li, F., Wu, S., Lin, F.R., Zhang, Z., Guan, Z., Yang, Z., Lee, C.-S., and Jen, A.K.Y. (2022). Co-assembled Monolayers as Hole-Selective Contact for High-Performance Inverted Perovskite Solar Cells with Optimized Recombination Loss and Long-Term Stability. Angew. Chem. Int. Ed. *61*, e202203088. https://doi.org/10.1002/anie.202203088.

42. Wang, G., Zheng, J., Duan, W., Yang, J., Mahmud, M.A., Lian, Q., Tang, S., Liao, C., Bing, J., Yi, J., et al. (2023). Molecular engineering of hole-selective layer for high band gap perovskites for highly efficient and stable

perovskite-silicon tandem solar cells. Joule *7*, 2583–2594. https://doi.org/10.1016/j.joule.2023.09.007.

43. Fei, C., Kuvayskaya, A., Shi, X., Wang, M., Shi, Z., Jiao, H., Silverman, T.J., Owen-Bellini, M., Dong, Y., Xian, Y., et al. (2024). Strong-bonding hole-transport layers reduce ultraviolet degradation of perovskite solar cells. Science *384*, 1126–1134. https://doi.org/10.1126/science.adi4531.
44. Lin, Y., Zhang, Y., Zhang, J., Marcinskas, M., Malinauskas, T., Magomedov, A., Nugraha, M.I., Kaltsas, D., Naphade, D.R., Harrison, G.T., et al. (2022). 18.9% efficient organic solar cells based on n-doped bulk-heterojunction and halogen-substituted self-assembled monolayers as hole extracting interlayers. Adv. Energy Mater. *12*, 2202503. https://doi.org/10.1002/aenm.202202503.
45. Al-Ashouri, A., Köhnen, E., Li, B., Magomedov, A., Hempel, H., Caprioglio, P., Márquez, J.A., Morales Vilches, A.B., Kasparavicius, E., Smith, J.A., et al. (2020). Monolithic perovskite/silicon tandem solar cell with 29% efficiency by enhanced hole extraction. Science *370*, 1300–1309. https://doi.org/10.1126/science.abd4016.
46. Li, C., Zhang, Z., Zhang, H., Yan, W., Li, Y., Liang, L., Yu, W., Yu, X., Wang, Y., Yang, Y., et al. (2024). Fully Aromatic Self-Assembled Hole-Selective Layer toward Efficient Inverted Wide-Bandgap Perovskite Solar Cells with Ultraviolet Resistance. Angew. Chem. Int. Ed. *63*, e202315281. https://doi.org/10.1002/anie.202315281.
47. McGrane, S.D., Barber, J., and Quenneville, J. (2005). Anharmonic Vibrational Properties of Explosives from Temperature-Dependent Raman. J. Phys. Chem., A *109*, 9919–9927. https://doi.org/10.1021/jp0523219.
48. Kumar, J., Patbhaje, U., and Shrivastava, M. (2022). Breathing Mode's Temperature Coefficient Estimation and Interlayer Phonon Scattering Model of Few-Layer Phosphorene. ACS Omega *7*, 43462–43467. https://doi.org/10.1021/acsomega.2c03759.
49. Wang, C.H., and Storms, R.D. (1971). Temperature-Dependent Raman Study and Molecular Motion in l-Alanine Single Crystal. J. Chem. Phys. *55*, 3291–3299. https://doi.org/10.1063/1.1676579.
50. Zhao, K., Liu, Q., Yao, L., Değer, C., Shen, J., Zhang, X., Shi, P., Tian, Y., Luo, Y., Xu, J., et al. (2024). peri-Fused polyaromatic molecular contacts for perovskite solar cells. Nature *632*, 301–306. https://doi.org/10.1038/s41586-024-07712-6.
51. Krückemeier, L., Krogmeier, B., Liu, Z., Rau, U., and Kirchartz, T. (2021). Understanding Transient Photoluminescence in Halide Perovskite Layer Stacks and Solar Cells. Adv. Energy Mater. *11*, 2003489. https://doi.org/10.1002/aenm.202003489.
52. Krogmeier, B., Staub, F., Grabowski, D., Rau, U., and Kirchartz, T. (2018). Quantitative analysis of the transient photoluminescence of CH3NH3PbI3/PC61BM heterojunctions by numerical simulations. Sustain. Energy Fuels *2*, 1027–1034. https://doi.org/10.1039/C7SE00603A.
53. Khenkin, M.V., Katz, E.A., Abate, A., Bardizza, G., Berry, J.J., Brabec, C., Brunetti, F., Bulović, V., Burlingame, Q., Di Carlo, A., et al. (2020). Consensus statement for stability assessment and reporting for perovskite photovoltaics based on ISOS procedures. Nat. Energy *5*, 35–49. https://doi.org/10.1038/s41560-019-0529-5.